Title

Numerical Experiments on Convective Heat Transfer in Water-Saturated Porous Media at Near-Critical Conditions

Journal

Transport in Porous Media, 5

Authors

Cox, B.L.
Pruess, K.

Publication Date

1988-09-01

LBL-26060
Preprint

Lawrence Berkeley Laboratory
UNIVERSITY OF CALIFORNIA

EARTH SCIENCES DIVISION

Submitted to International Journal of Heat and Mass Transfer

Numerical Experiments on Convective Heat Transfer in Water-Saturated Porous Media at Near-Critical Conditions

B.L. Cox and K. Pruess

September 1988

Prepared for the U.S. Department of Energy under Contract Number DE-AC03-76SF00098.

DISCLAIMER

Numerical Experiments on Convective Heat Transfer in Water-Saturated Porous Media at Near-Critical Conditions

B.L. Cox and K. Pruess

Earth Sciences Division
Lawrence Berkeley Laboratory
1 Cyclotron Road
Berkeley, California 94720

Abstract

Fluid and heat flow at temperatures approaching or exceeding that at the critical point (374°C for pure water, higher for saline fluids) may be encountered in deep zones of geothermal systems and above cooling intrusives. In the vicinity of the critical point the density and internal energy of fluids show very strong variations for small temperature and pressure changes. This suggests that convective heat transfer from thermal buoyancy flow would be strongly enhanced at near-critical conditions. This has been confirmed in laboratory experiments.

We have developed special numerical techniques for modeling porous flow at near-critical conditions, which can handle the extreme non-linearities in water properties near the critical point. Our numerical simulations show strong enhancements of convective heat transfer at near-critical conditions; however, the heat transfer rates obtained in the simulations are considerably smaller than data reported from laboratory experiments by Dunn and Hardee. We discuss possible reasons for this discrepancy and develop suggestions for additional laboratory experiments.

INTRODUCTION

Fluid conditions approaching or exceeding the critical point (374 °C, 221 bars for pure water, higher temperatures and pressures for saline brines) may be reached in the deep ends of geothermal systems such as Mofete [1] and Larderello [2], as well as above crustal magma bodies. Yet, little is known about how heat and fluid flow are affected by critical conditions. In order to better evaluate geothermal reservoirs with critical conditions at depth, and to estimate heat and fluid flow in critical zones above magma bodies, we need to better understand the behavior of geothermal fluids near the critical point.

Previous studies include one by Cathles [3] who used a finite-difference model to study cooling igneous intrusives and the formation of liquid and vapor-dominated geothermal systems, as well as the formation of porphyry type ore deposits. He concluded that fluids circulate around the critical point of water to become gaseous without boiling, and that these zones are potentially exploitable. Norton and Knight [4] also performed finite difference simulations of cooling plutons, finding that the style of circulation was controlled by the critical fluids and that the total heat flow calculations can be significantly in error if these convecting zones are not considered.

Laboratory experiments of natural convection of near-critical fluids in a porous medium were performed by Dunn and Hardee [5] for water, and by Hadley [6] for carbon dioxide. Dunn and Hardee concluded from their measurements that heat transfer rates increased by factors of up to 70 when compared to conductive heat flow near the critical point of water, and attributed this enhancement to the extreme behavior of fluid properties (especially density and heat capacity) in the critical region. Hadley [6] found substantial heat transfer enhancement (Nusselt number of 12) for carbon dioxide,

and concluded that thermal dispersion was very important because of high fluid velocities generated near the critical point.

Above critical temperatures and pressures, there are no longer distinct liquid and gas phases, but instead a continuous variation from liquid-like fluid to gas-like fluid. This supercritical fluid has an enhanced ability to transport heat by convection because of the extreme behavior of fluid properties such as density and heat capacity. The driving forces for thermal buoyancy flow are magnified by the strong changes of fluid density for relatively small changes in temperature and pressure. Additional enhancement of convective heat transfer occurs from the large specific heat. Contours of density and of internal energy at near-critical temperatures and pressures are plotted on Figures 1a and 1b. These plots were made by using a table generated from the Haar equation of state [7]. The rapid changes in values indicated by the bands of compressed contours show one of the many obstacles to overcome when trying to model a system with such rapidly changing fluid properties.

In the present paper we study flows at slightly supercritical pressures that do not involve phase transitions. We examine in some detail the experimental results on near-critical porous convection obtained by Dunn and Hardee [5], finding some inconsistencies which, for lack of a sufficiently detailed definition of experimental conditions cannot be resolved. Consequently no quantitative validation of our numerical simulator for near-critical flow was possible. We then present a series of numerical experiments to gain insight into conditions and parameters controlling near-critical heat transfer.

NUMERICAL MODELING OF NEAR-CRITICAL FLOW

Simulations were performed with the geothermal reservoir simulator MULKOM [8, 9], which is based on an integral finite difference discretization [10] of the general transient conservation equations for flow in a homogeneous porous medium. For single phase conditions, these can be expressed as (for an explanation of symbols see the nomenclature):

$$\frac{\partial \phi \rho}{\partial t} = -\mathrm{div}(\rho \underset{\sim}{v}) \qquad \text{Mass conservation} \tag{1}$$

$$\underset{\sim}{v} = -\frac{k}{\mu}(\nabla P - \rho \underset{\sim}{g}) \qquad \text{Momentum} \tag{2}$$

$$\frac{\partial [(\rho C_p)_m T]}{\partial t} = \lambda_m \nabla^2 T - \mathrm{div}\{(\rho C_p)_f T \underset{\sim}{v}\} \qquad \text{Energy} \tag{3}$$

The simulator equations do not include thermal dispersion effects [11]; these will be examined below. Rapid variations in the water properties near the critical point create problems for numerical models, necessitating the development of new techniques. The equation of state developed by Haar et al. [7] was used to represent the thermophysical properties of water. Because the full Haar et al. formulation involves many highly non-linear terms with significant numerical cancellation in the near-critical region, we did not use it directly in the simulator. Instead, we calculated a two-dimensional table from the formulation given by Haar et al., of densities and internal energies as functions of temperature and pressure in the critical region. A bi-linear interpolation scheme is used to estimate values between table values.

The presence of large pressures and small pressure differentials near the critical point makes it difficult to obtain the required high accuracy for the pressure differences that drive flow between neighboring finite-difference grid cells. The numerical cancellations occurring in computations of pressure differences are particularly severe when one attempts to model flow processes on a (small) laboratory scale, where pressure variations are much smaller than would be encountered in much larger-scale hydrothermal convection systems in the subsurface. For example, in the simulations reported below, typical pressure differences between neighboring grid cells at spacings from 1 to 10 mm are of order 10 Pa, which is a factor of 10^{-6} smaller than the absolute pressure. This problem was overcome by measuring pressure relative to a floating reference pressure, taken to be the average pressure in the flow system at each time step, so that more significant figures could be retained when computing pressure differences.

Another problem was encountered when initializing a thermal convection problem with uniform temperature throughout the porous medium. This gave rise to many transient flow reversals and the approach to steady state was very slow and costly in computer time. In the present work we are only interested in the steady state attained after all transient changes have disappeared. To speed up the approach to steady state, we initialized the simulations by generating a set of temperatures corresponding to pure steady conduction between the heat source and the outer constant temperature boundary. This conductive steady state initialization greatly improved the efficiency of the simulations.

EXPERIMENTAL DATA

Before the simulator can be used to model geologic systems, it should be validated against some experimental data. The only available experimental work on near-critical convection of water in porous media is the one performed by Dunn and Hardee [5]. A conceptual sketch of the experimental setup is shown in Fig. 2. A 1 liter

cylindrical vessel filled with a fine silica sand was heated with electrical tape heaters on the cylinder mantle, and along a thin platinum wire in the center of the vessel. The outside of the cylinder was kept at a somewhat lower temperature than the wire, and the top and bottom of the cylinder were insulated. Pressures ranged from 225 to 248 bars (22.5 to 24.8 MPa). The steady-state temperatures were measured with embedded thermocouples, and the total heat transfer divided by conductive heat transfer (Nusselt Number, Nu) was estimated. The experimenters found an enhancement in heat transfer in a broad temperature range from 360 °C to 400 °C, which near the critical point reached a peak of about 70 times that for pure conduction.

Dunn and Hardee [5] estimated Rayleigh numbers for parameters representative of their experiment, using a hypothetical temperature difference of 2 °C between the wire and the cylinder mantle, where

$$Ra = \frac{kg\alpha\Delta TH}{\kappa_m \nu} \approx \frac{kg\bar{\rho}\bar{C}_p H(\rho_o - \rho_i)}{\mu\lambda_m} \qquad (4)$$

Using the cylinder height as the characteristic length dimension, they found a narrow peak of approximately 2 °C width at half maximum centered at 374 °C with maximum Rayleigh number of 700. The experimental measurements, when plotted as rate of heat transfer per unit temperature drop between two measurement points in the vessel, showed a temperature dependence simular to, although much broader than, that of the calculated Rayleigh numbers. This correspondence led Dunn and Hardee [5] to suggest that the enhanced heat transfer near the critical point was in fact brought about by enhanced convection. Nu is usually proportional to Ra; however, the calculated Rayleigh numbers of Dunn and Hardee [5] are much too small to explain the observed heat transfer enhancements by factors up to 70. If different length scales were used in the calculation of the Raleigh number, as described by other authors, the expected Nu should be between 2 and 5 [12, 13, 14], not 70. Another puzzling feature of the

experimental results is that measured heat transfer is strongly enhanced over a rather broad temperature interval (from 360 ° to 400 °C), while the peak in the Rayleigh numbers (for a 2 °C temperature difference) is very narrow and steep right at the critical temperature.

A Rayleigh number based on average temperature differences between hot and cold boundaries seems not a very meaningful measure of convective heat transfer in a flow system with cylindrical symmetry, because temperature behaves in singular fashion near the symmetry axis. Furthermore, we believe that the method of estimating Nu in the experiment may have given misleading results. The precise location of the temperature sensors is not given by Dunn and Hardee, but from the sketch in their paper, it appears that the temperature measurements were made at the mid-height of the vessel, at some distance from the heater wire. When convection occurs, a thin boundary layer forms next to the wire, and the pattern of convection is asymmetrical in the vertical direction, so that these temperature measurements would not permit quantitatively accurate estimates of the Nusselt number.

We conclude that the experiment of Dunn and Hardee [5] does not provide a sufficiently detailed definition of thermodynamic conditions in the flow system and on its boundaries to permit a detailed code validation.

RESULTS OF SIMULATIONS

Using the flow geometry shown in Figure 2, a series of numerical experiments were performed to study various issues relating to near-critical heat transfer. We examined effects of boundary conditions, aspect ratio of convecting cells, space discretization, average temperature, temperature interval, thermal dispersion, and flow channeling. Simulation parameters and results are given in Tables 1-7 and in Figures

3-7. Our initial simulations gave rather weak enhancements in overall heat transfer, and we made specific efforts to find conditions that would give more enhanced heat transfer, using flow geometry and parameters similar to those of the Sandia experiment. A radial section showing nodal point locations for the two-dimensional axisymmetric grid used in most simulations is shown in Figure 3. The convection flow directions were similar in all simulations; an example is given in Figure 4.

Boundary Conditions

For most of the simulations the following boundary conditions were imposed: all boundaries are impervious to fluid flow, with constant temperature along the innermost elements and on the cylinder mantle, and perfectly insulated boundaries on top and bottom of the vessel. Temperature differences between cylinder axis and mantle were maintained at 2 °C. Typical isotherm patterns for conduction only, and for convection, are shown in Figures 5a and 5b, respectively. We also examined the case of constant temperature at the top and bottom boundaries, and although the isotherms are different (Figures 5c and 5d), the average heat flow is not very much changed (Table 2).

An experimental study by Prasad and others [14] showed that for natural convection in a porous annulus the value of Nu obtained for an isothermally heated annulus is 10 to 30% lower than that for a constant heat flux. They observed that a change in boundary conditions from constant temperature to constant heat flux results in a much thinner thermal boundary layer on the inner wall. However, the differences between the two types of boundaries decrease with increasing Rayleigh number. We performed calculations with uniform heat flux as well as with constant temperature at the wire heater and found no significant difference in total heat flow rate.

Discretization Effects

Discretization effects result from two sources: from the spacing of the grid points, and from the interpolation of densities and internal energies from tabular data for discrete pressure and temperature values. The first type of discretization effect was noticeable even when using grid blocks with less than 1 mm linear dimensions (see Figure 3). Cases 4 and 5 (Table 2) were identical, except that case 5 had an extra grid point next to the hot wire, to provide improved spatial resolution in the region where discretization effects are strongest. The addition of the extra grid point actually decreased the Nusselt number slightly.

Discretization effects resulting from the tabulation of water properties were not very great, but could be significant for a small temperature interval at the critical point. For most of the cases, a table with .1 bar pressure intervals and .1 °C temperature intervals was used. For comparison, another table was used in some of the simulations having a pressure interval of 1 bar, and a temperature interval of .05 °C (see Table 2), and case 1 was rerun with this table. For a permeability of 40 D, the Nusselt number was 2.1 instead of 2.2. For larger temperature intervals this effect was almost unnoticeable.

Aspect Ratio of Convection Cells

Dependence of heat transfer on the aspect (radius : height) ratio was studied, since the actual geometry of the convecting cells is unknown. These results are shown in Figures 6 and 7 and Table 3. For a permeability of 40 D, the Nusselt number for a radius to height ratio of 1:6 (that of the Sandia experiment) was 2.2, while for a ratio of 2:1, the Nusselt number was 4.8, over twice as large. Thus heat transfer increases considerably with aspect ratio, especially for small aspect ratios (Figure 7).

An obvious question arising from these results is the stability of multiple cell convection, where one or more short cells would be stacked on top of one another, resulting in larger heat transfer than for a single cell. For a rectangular geometry with heat transfer in the vertical direction, it is known that convection cells will evolve such as to maximize heat transfer [15]. If shorter convection cells maximize heat transfer, would a stacking of several cells be stable for the vertical cylinder geometry?

Consider a state as depicted in Figure 8 which has two identical convection cells stacked atop one another. At time t=0, the boundary between the two cells is removed. The subsequent pressure and temperature response can be inferred from an examination of the relevant diffusivities for fluid flow and heat conduction. The pressure diffusivity

$$D_P = k/\mu\phi\beta \tag{5}$$

for typical parameters, ($k = 4 \times 10^{-11}$ m^2, $\phi = 25\%$, T = 376 °C, P = 225.5 bars, $\beta = 3.74 \times 10^{-7}$ /Pa, $\mu = 3.03 \times 10^{-5}$ Pa-s) is 14 m^2/s. From elementary considerations the time needed for pressure change to travel from the middle to the top of the cylinder, can be estimated as [16]:

$$t_P = \frac{x^2}{D_P} \cdot \tag{6}$$

For x = 0.1 m as in the Sandia experiment, this is very rapid, approximately 10^{-3} sec. By comparison, the thermal diffusivity,

$$\kappa_m = \lambda_m/(\rho C_p)_f \tag{7}$$

is 2.8×10^{-7} m^2/s (for $\lambda_m = 2.5$ W/m °C, $\rho_f = 205.1$ kg/m^3, $C_{pf} = 44.27$ kJ/kg °C), showing that conductive temperature changes will propagate much more slowly. The characteristic time for heat conduction is

$$t_T = \frac{x^2}{\kappa_m}, \tag{8}$$

so that penetration over 0.1 m requires approximately 4×10^4 sec. Note that the thermal diffusivity defined in Equation 7 is based on a mixture of fluid properties and porous medium properties. Katto and Masuoka [17] suggested that this is the appropriate thermal diffusivity to use, based on theory and experiments; their formulation was adopted by other researchers [18, 6].

Results from numerical simulations with a double cell as initial condition confirmed the analysis above. We found that the two cells rapidly achieved pressure equilibration due to gravity forces, breaking the double cell flow configuration within fractions of a second, before any noticeable temperature change occurred. Pressures were initialized for the double-cell initial conditions so that the average vertical pressure gradient was smooth, increasing downwards. Near the contact between the two cells (dashed line in Figure 8) flow is initially directed outward in the lower cell, inward in the upper. The pressure differences associated with these flows are such that an upward flow across the contact between the two cells is induced near the heater, while near the mantle downward flow occurs. These crossflows rapidly break the double-cell pattern and initiate a single-cell flow pattern. However, within the adjacent layers of the upper and lower cell, the pressure gradient near the wire for the lower cell is higher than that of the upper cell, driving net gradient upwards. The situation is reversed on the mantle side, with a net pressure gradient downwards. These vertical pressure gradients are on the order of 3 or 4 Pa, but are sufficient to immediately initiate single-cell concentration from the time-zero fluxes. The initial temperature distribution where a lower temperature at the bottom of the upper cell is adjacent to the higher temperature at the top of the bottom cell is also unstable thermally. However, the temperature contours do not stabilize into the single cell configuration until a period of about 10^5 sec.

Studies for horizontal layer geometries have shown that with increasing Rayleigh number, transitions to chaotic flow occur, with transitions to intermediate oscillatory periodic flows at Rayleigh numbers of around 400 [19]. In these intermediate stages, symmetry is destroyed and multiple cells are formed. If heat transfer in the Sandia experiment had been in fact enhanced by factors as large as 70 [1], the corresponding Rayleigh numbers would have to have been very large (>>400) and transitional or even chaotic convection would have occurred. The actual Rayleigh numbers (Figure 6), computed using average thermal properties and the radius or gap width as the length scale, are ~ 300 and ~ 600 for permeabilities of 20 and 40 Darcy. Other dimensional numbers affecting the stability of laminar convection are the Prandtl and Reynolds numbers which are very small for this problem, being approximately 1 and .1, respectively. Therefore, the experimental parameters do not indicate chaotic convection based on analysis of dimensionless numbers.

Size of Temperature Interval

Effects of the temperature interval on convective heat transfer were examined by using a 10 °C temperature difference between the wire and the cylinder mantle, rather than a 2 °C difference. The Nusselt number for a permeability of 40 darcies was only 1.5, considerably less than had been obtained with the smaller temperature difference. This was to be expected, since for a larger temperature interval across the system the region with strongest convective enhancement near the critical point is reduced in volume.

Another case was simulated with a 1 °C temperature difference between the wire and the cylinder wall. The results were very similar to those for a 2 °C temperature difference (see Table 4).

Temperature Dependence

Dunn and Hardee [5] displayed their experimental results in a graph of normalized heat transfer versus average temperature. In their experiments, normalized heat transfer (Nu) greater than 10 was observed for temperatures in the range between 365 °C and 400 °C, with a broad maximum of Nu ≈ 70 over a 20 °C interval between 380 °C and 400 °C.

Simulations with average temperatures between 360 °C and 380 °C were performed to examine the temperature dependence of heat transfer. The temperature difference between cylinder axis and mantle was 2 °C, and an average pressure of 225 bars was applied, equal to the lowest pressure used in the Sandia experiment. The results are shown on Figure 9, where log (Nu - 1) is plotted as a function of the average temperature for permeabilities of 20 and 40 Darcy. For a pressure of 225 bars, the heat transfer enhancement from near-critical properties peaks at a temperature of 376 °C and is only significant in a very small temperature range of about 2.5 °C. The temperature and pressure conditions with maximum heat transfer fall on the line of maximum heat capacity, as shown in Figure 10. (Note that this line joins smoothly with the saturated vapor pressure line at sub-critical temperatures.) In this figure we have also drawn contour lines for heat capacities of 133 and 20 kJ/kg · °C to emphasize the narrowness of the region with extreme property variations. For temperatures beyond 376 °C, heat transfer drops off much less rapidly when pressures are also increased to follow the line of maximum heat capacity than if pressures are kept constant (see Figure 9). This observation suggests that in geothermal systems, conditions of near-critical enhanced heat transfer could occur over large depth intervals, if pressures and temperatures would remain near the line of maximum heat capacity as shown in Figure 10.

Flow Channeling

The porosity of packed equal-sized spheres increases next to a boundary, creating flow paths with greater permeability [20, 21]. This "channeling" effect depends on many factors such as grain size and shape, grain size distribution, and curvature of the boundary. The porosity distribution of packed spheres in a cylinder was studied by Benenati and Brosilow [20]. They observed that porosity approached 1 near the wall, decreasing away from the wall in a damped oscillatory wave over a distance of approximately 4.5 to 5 sphere diameters. Vafai and Tien [22] estimated that for a vertical plate, Nu could be more than doubled by flow channeling. Tokunaga [23] estimated analytically the error in permeability measurements arising from annular wall flow, assuming a parabolic velocity profile through the gap. He found that channeling could enhance flux in a gap of 10 micron width by as much as a factor of 10.

Effects of channeling for the flow geometry shown in Figure 2 can be simulated by specifying enhanced permeability near the wire heater and near the cylinder mantle. Because of the cylindrical geometry, channeling effects would be most important in the vicinity of the wire, where fluxes are much larger than near the mantle. The parameters used for reference case 1 (Table 1) were modified to examine channeling effects. Assuming that a tenfold increase in permeability would occur over a radial distance of 4 grain diameters from the wire (400 microns) in Dunn and Hardee's experiment, average permeability of the innermost column of gridblocks (radius 900 microns) would be enhanced by a factor 2.8. This enhancement resulted in an 17% increase in simulated heat transfer. If the velocities resulting from the flow channeling simulation are used to estimate dispersive heat flux (Equation 15), the total heat transfer might be as high as Nu = 3.2 (Table 7) , an enhancement of 42%.

THERMAL DISPERSION EFFECTS

Thermal dispersion is analogous to hydrodynamic dispersion and results from local velocity variations due to the mechanical interaction of the fluid with the porous medium structure [11]. Along the direction of average fluid flow, the heat-carrying fluid is diverted from a straight path because of the geometry of the pore channels. Instead of a sharp thermal front which would occur if there were no dispersion, the thermal front is spread or dispersed both along and perpendicular to the average flow direction in the same way a solute is dispersed in tracer experiments. The dispersion along the average fluid flow path is called the longitudinal dispersion, while the dispersion perpendicular to the average flow direction is called the transverse dispersion. Total dispersion increases with increasing velocity. For the heat transfer geometry considered here (Figure 2), transverse dispersion should give stronger effects than longitudinal dispersion, because transverse dispersion is primarily in the direction of overall heat transfer, i.e. from the heater wire to the walls, while longitudinal dispersion for this aspect ratio is primarily along the vertical direction, i.e., perpendicular to the main heat transfer.

Several researchers have observed that thermal dispersion may significantly enhance heat transfer. Kvernvold and Tyvand [18] studied theoretically the dispersion effects on thermal convection in a fluid-saturated porous layer bounded by two infinite horizontal planes at constant temperature. They considered incompressible flow (ρ = constant), for which the energy equation (Equation 3) can be simplified to give the following dimensionless form [11, 18].

$$\frac{\partial T_D}{\partial t_D} + \underset{\sim}{v}_D \cdot \nabla T_D = \nabla \cdot (\underline{\underline{D}}_D \cdot \nabla T_D) \tag{9}$$

Following Hadley [6] the appropriate unit of length for cylindrical flow geometry is radius R. The units of time t, velocity $\underset{\sim}{v}$, temperature T and pressure P are

$(C_p\rho)_m$ R^2/λ_m, κ_m/R, ΔT and $\rho \underset{\sim}{v} \kappa_m/k$, respectively. Following Kvernvold and Tyvand, the dimensionless dispersion tensor $\underline{\underline{D}}$, is written as

$$\underline{\underline{D}}_D = (1 + \varepsilon_2 v_D^2)\underline{\underline{I}} + (\varepsilon_1 - \varepsilon_2)\underset{\sim}{v}_D \underset{\sim}{v}_D \tag{10}$$

where $\underline{\underline{I}}$ is the unit tensor, and ε_1 and ε_2 are the coefficients of longitudinal and transverse dispersion, relative to the flow direction. These longitudinal and transverse dispersion coefficients are [18]:

$$\varepsilon_1 = \frac{b}{15} \; ; \; \varepsilon_2 = \frac{b}{40} \tag{11}$$

where the dispersion factor b is given by [18]:

$$b = \frac{\kappa_m}{\kappa_f}\frac{d^2}{R^2} = \frac{\lambda_m d^2}{\lambda_f R^2} \tag{12}$$

The parameter d is the characteristic pore or grain dimension and can be estimated with the capillary tube formula [6]

$$d = 2\sqrt{\frac{8k}{\phi}} \tag{13}$$

Here k is permeability and ϕ is porosity.

The dispersion factor b (Equation 12) is a dimensionless number which can be used to estimate the magnitude of the dispersion effects [18]. Dispersion effects increase with increasing Rayleigh number. For convection between infinite horizontal planes, Kvernvold and Tyvand found that dispersion effects were not significant until Ra exceeded about 200. Dispersion effects are also dependent on the ratio of the grain diameter to the thickness of the layer. Thus, if the thickness of the layer is large relative to the characteristic grain diameter, dispersion effects become insignificant.

The maximum effect of dispersion predicted by Kvernvold and Tyvand was to almost double Nu. Hong and Tien [24] and Hong, Yamada and Tien [21] analyzed theoretically the effects of thermal dispersion for a vertical heated plate embedded in a porous medium. Maximum dispersion effects could triple or quadruple the size of Nu.

Hadley [6] studied experimentally the thermal convection of CO_2 at near-critical conditions in a cylinder filled with fine silica sand, where the heat was transferred from an axial wire heater to constant temperature walls. The wall temperature was maintained at around 31 °C, slightly above critical temperature; a constant heat input was applied, and temperatures varied between 31 °C at the wall to 33.7 °C at the wire, depending on pressure. The dimensions of the cylinder were nearly identical to those of the Dunn and Hardee experiment. The pressures were lowered to near-critical, and dispersion became important only when the ratio P/P_c (pressure divided by critical pressure) was less than 1.01. Dispersion effects were dominant when the pressure ratio was less than 1.005. The maximum effect of dispersion approximately doubled Nu, but this only occurred very close to the critical point, where a maximum Nu of 12 was obtained.

We proceed to make an approximate estimation for dispersive heat flux for the problem studied in the numerical simulations above. The simplest approach toward such an estimate is to use the simulated velocity patterns to estimate dispersive flux, based on the formulation given by Kvernvold and Tyvand [18]. Their expression for dispersive heat transfer was derived under the assumption of incompressible flow of a fluid with small expansivity. These assumptions are not well justified near the critical point; however, we are analyzing flow systems in which overall differences in temperatures and pressures are small, so that variations in compressibility and expansivity will be limited.

The sum of conductive and dispersive heat flux $\underset{\sim}{G}$ can be expressed in dimensional form as

$$\underset{\sim}{G} = -\lambda_m \underset{=}{D}_D \cdot \nabla T \tag{14}$$

From Equations 10 and 14 we obtain for the dispersive heat flux in the radial direction

$$\underset{\sim}{G}_{dis,r} \equiv -\lambda_m (\nabla T)_r \left(\frac{R}{\kappa_m}\right)^2 (\varepsilon_2 v_z^2 + \varepsilon_1 v_R^2) \tag{15}$$

From Equations 10, 14, and 15, it is seen that the dispersive heat flux in the radial direction can be interpreted as enhancing effective thermal conductivity $\lambda_m \rightarrow \lambda_m' = \lambda_m(1 + f)$, where

$$f = \left(\frac{R_o}{\kappa_m}\right)^2 (\varepsilon_2 v_z^2 + \varepsilon_1 v_R^2) \tag{16}$$

The velocity in the r-direction, v_r, will be small except at the top and bottom of the cylinder, so that the result can be further simplified to

$$f \simeq \left(\frac{R}{\kappa_m}\right)^2 \varepsilon_2 v_z^2 \tag{17}$$

With this approximation the Nusselt number including dispersive heat flux can be estimated as

$$Nu = \frac{G_{tot}}{G_{cond}} = \frac{\tilde{G} + G_{conv}}{G_{cond}} \tag{18}$$

where

$$\tilde{G} = \frac{\log R_o/R_i}{\int_{Ri}^{Ro} \frac{dR}{R(1+f)}} G_{cond} \tag{19}$$

is the sum of conductive and dispersive heat flow in the radial direction. The

parameters and resulting pore velocities obtained from the reference case simulation (Table 12), were used to estimate Nu from Equations 18 and 19. The integral in the denominator of Equation 19 was calculated numerically from the values of R and f at each grid point, using the actual simulated velocities and thermal properties along the mid-height of the cylinder. Results are given in Table 6. The addition of the dispersive flux increased Nu from 2.2 to 2.6, an increase of 16%. This enhancement is in the range of dispersion efforts predicted by other researchers [24, 6]. If the velocities including flow-channeling effects are used to estimate dispersion, Nu is increased to 3.2. This enhancement is in the range of dispersion effects predicted by Hong and Tien [24] for the vertical plate. Thus, dispersion is found to give modest increases of Nu, but it does not provide a mechanism by which the near-critical enhancement in heat transfer could be spread over a larger temperature interval.

DISCUSSION AND CONCLUSIONS

We have developed special numerical techniques to model convective heat transfer at near-critical conditions. Stable steady states were achieved for model systems with linear dimensions of the order of .1 m, with spatial resolutions better than 1 mm and pressure differences of order 10 Pa between neighboring finite difference grid cells.

No validation of the numerical model was possible because the only available experiment on near-critical porous flow of water [5] lacks sufficiently detailed definition of thermodynamic conditions. Numerical experiments for a flow system similar to that studied by Dunn and Hardee showed significantly enhanced heat transfer near the critical point, if a permeability 20 times greater than that reported in the laboratory experiments is used. However, the enhancements seen in the simulations (up to a factor 5 over pure conduction) are substantially smaller than was observed in the laboratory experiments (up to a factor 70). Furthermore, the simulations predict significant heat transfer enhancement only for a narrow temperature interval (a few °C), while Dunn and Hardee reported enhancement over a broad range (20 °C). While we did not expect detailed agreement, a discrepancy that large is surprising. Various effects that could enhance heat transfer in the numerical model were examined, which are summarized below. None of these effects could increase heat transfer to nearly as large values as were reported by the experimenters.

Discretization and boundary effects were very small, of the order of a percent. The study of aspect ratios showed that short stacked cells could enhance heat transfer significantly, by a factor of as much as 5, but a study of the stability of stacked cells

indicated that this configuration would be unstable. A study of the size of the temperature interval showed how the temperature difference bears no direct relationship to Nu in the critical region, and contrary to convection in non-critical conditions, a smaller temperature interval can result in a higher Nu than a larger temperature difference.

If average pressure is kept constant, the numerical simulation shows enhanced heat transfer effects only over a very small temperature interval. Dunn and Hardee observed enhanced heat transfer over a very large temperature interval (> 20 °C), which may reflect that pressures were not constant. If pressures were increased with temperature to remain near the line of maximum specific heat (Figure 9), the critical effects would occur over a broader range of temperatures.

Another possible mechanism for enhanced heat transfer is flow in channels of high permeability near the wire heater. We estimated that channeling effects from packing of spherical grains along a flat boundary could increase the total heat transfer rate by as much as 17%. Additional enhancement could occur from dissolution of quartz near the wire [25, 26].

Transversal dispersion [18, 6] can have significant effects for the cylindrical flow geometry considered here, because it produces a component of velocity in the direction of overall heat transfer (radial). Estimates of dispersion alone raised the Nu to 2.6 for the reference case, and a combination of dispersion and flow channeling resulted in a Nu of 3.2, still much less than that seen by Dunn and Hardee. In his experiments with CO_2, Hadley found a maximum Nu = 12 in immediate proximity to the critical point.

The apparent discrepancy between the rather modest heat transfer rates seen in the numerical simulations and the very large heat transfer enhancement inferred by Dunn and Hardee from their experimental data could perhaps be due to the pronounced

vertical asymmetry of the temperature field (see Figures 5b and 5d). A thermocouple placed near the center of the flow region would register only a slightly higher temperature in the convective state (Figure 5b) than in the conductive state (Figure 5a). In the convective state shown in figure 5d temperature near the center would in fact be lower than in the purely conductive state portrayed in Figure 5c, even though overall heat transfer is enhanced. If placed below the center, temperatures in the convective regime would generally tend to be lower than for purely conductive heat transfer. The conclusion form these observations is that temperative difference between an imbedded themocouple and the outer cylinder wall (mantle) may be a poor and unreliable measure of conductive heat flow. The asymmetry of the temperature field under convecting conditions is such as to yield a systematic underestimate of conductive heat transfer, so that exaggerated Nusselt numbers may be inferred from these data.

If we use simulated temperatures for the cases shown in Figures 5b and 5d at a point in the midplane, near 2/3 of cylinder radius, to estimate heat transfer enhancement following Dunn and Hardee's approach, we find apparent enhancements if 8.67 and 9.42, respectively, compared with actual Nusselt numbers of 2.06 and 2.08.

We suggest that additional carefully controlled and instrumented laboratory experiments should be undertaken to better define the physical conditions and mechanisms for near-critical heat transfer. The cylindrical geometry employed by Dunn and Hardee [5] is complicated by singular behavior at small radius, with the undesirable feature that flow behavior may be strongly influenced by conditions (heterogeneities, etc.) on a very small spatial scale. From the standpoint of ease of interpretation a linear flow geometry would be most desirable, but this appears difficult to realize experimentally. The best configuration for experimental studies may be a porous annulus, where the inner radius is not very much smaller than the outer radius, so that a non-singular and approximately linear flow geometry may be achieved.

Acknowledgement

The authors gratefully acknowledge valuable discussions and suggestions from Robert McKibbin, University of Auckland, New Zealand. Thanks are due to Drs. Robert Zimmerman, Pascal Bidaux and Joseph Wang for critical review of the manuscript. This work was supported by the Geothermal Technology Division, U.S. Department of Energy, under Contract No. DE-AC03-76SF00098.

Nomenclature

b	Dispersion factor, dimensionless
C_p	Specific heat at constant pressure, kJ/kg °C
$\underline{\underline{D}}$	Dispersion tensor, dimensionless
D_p	Pressure diffusivity, m^2/s
d	Characteristic pore (or grain) dimension, m
f	Dispersive enhancement factor, dimensionless (Equation 17)
g	Gravity acceleration, 9.8 m/s^2
G	Heat flux, W/m^2
h	Enthalpy, kJ/kg
H	Height, m
k	permeability, m^2(or darcy $\approx 1 \times 10^{-12}$ m^2)
Nu	Nusselt number, dimensionless
P	Pressure, Pa (or bar = 10^5 Pa)
R	Radius, m
Ra	Rayleigh number, dimensionless
t	Time, sec
T	Temperature, °C
v	Velocity, m/s
x	Distance, m

α	Coefficient of thermal expansion, $°C^{-1}$
β	Compressibility, $/Pa^{-1}$
κ	Thermal diffusivity, m^2/s
λ	Thermal conductivity, W/m °C
μ	Dynamic viscosity, $Pa \cdot s$
ρ	Density, kg/m^3
ν	Kinematic viscosity, m^2/s
ϕ	Porosity, dimensionless

Subscripts

c	Critical
cond	Conductive
conv	Convective
dis	Dispersive
f	Fluid
i	Inner
m	Medium
o	Outer
p	Pressure
r	Radial
R	Rock
t	Temperature
tot	Total
w	Wire

z	In z-direction

Units for Non-Dimensional Parameters

length	R
time	$(C_p \rho)_m R^2/\lambda_m$
velocity	κ_m/R
Temperature	ΔT
Pressure	$\rho\nu\kappa_m/k$

References

1. Facca, G., Geothermal Activity in Italy, *Geothermal Resources Council Bulletin,* January 1985, 10-14 (1985).

2. Cappetti, G., Celati, R., Cigni, U., Squarci, P., Stefani, G., and Taffi, L., Development of Deep Exploration in the Geothermal Areas of Tuscany, Italy, 1985 International Symposium on Geothermal Energy, International Volume, Geothermal Resources Council, 303-309 (1985).

3. Cathles, L.M., An Analysis of the Cooling of Intrusives by Groundwater Convection which Includes Boiling, *Econ. Geol.,* **72,** 804-826 (1977).

4. Norton, D. and Knight, J., Transport Phenomena in Hydrothermal Systems and Cooling Plutons, *Am. J. Sci.,* **77,** 937-981 (1977).

5. Dunn, J.C. and Hardee, H.C., Superconvecting Geothermal Zones, *J. Volcanol. and Geotherm. Res.,* **11,** 189-201 (1981).

6. Hadley, G.R., Natural Convection of a Near Critical Fluid through a Porous Medium, Sandia Report SAND82-1072J (1982).

7. Haar, L., Gallagher, J.S., Kell, G.S., NBS/NRC Steam Tables, Hemisphere Publishing Corp. (1984).

8. Pruess, K., Development of the General Purpose Simulator MULKOM, Annual Report 1982, Earth Sciences Division, Report LBL-15500, Lawrence Berkeley Laboratory (1983).

9. Pruess, K., SHAFT, MULKOM, TOUGH: A Set of Numerical Simulators for Multiphase Fluid and Heat Flow, *Geotermia, Rev. Mex. Geoenergia,* **4,** 185-202, (1988).

10. Narasimhan, T.N. and Witherspoon, P.A., An Integrated Finite Differences Method for Analyzing Fluid Flow in Porous Media, *Water Resources Research,* **12,** 57-64 (1976).

11. Bear, J., Dynamics of Fluids in Porous Media, *Elsevier* (1972).

12. Bejan, A., Convection Heat Transfer, John Wiley and Sons, p. 398, (1984).

13. Reda, D.C., Natural Convection Experiments with a Finite-Length, Vertical Cylindrical Heat Source in a Water-Saturated Porous Medium, *Nuclear and Chemical Waste Management*, **6**, 3-14 (1986).

14. Prasad, V., Kulacki, F.A. and Kulkarni, A.V., Free Convection in a Vertical, Porous Annulus with Constant Heat Flux on the Inner Wall - Experimental Results, *Int. J. Heat Mass Transfer*, **29**, 713-723 (1986).

15. Platzman, G.W., The Spectral Dynamics of Laminar Convection, *J. Fluid Mech.*, **23**, 481-510 (1965).

16. Carslaw, H.S., and Jaeger, J.C., Conduction of Heat in Solids, Oxford University Press, 2nd Ed., (1959).

17. Katto, Y. and Masuoka, T., Criterion for the Onset of Convective Flow in a Fluid in a Porous Medium, *Int. J. Heat Mass Transfer*, **10**, 297-309 (1967).

18. Kvernvold, O., and Tyvand, P., Dispersion Effects on Thermal Convection in Porous Media, *J. Fluid Mech.*, **99**, 673-686 (1980).

19. Kimura, S.G., Schubert, G. and Straus, J.M., Route to Chaos in Porous-Medium Thermal Convection, *J. Fluid Mech.*, **166**, 305-324 (1986).

20. Benenati, R.F. and Brosilow, C.B., Void Fraction Distribution in Beds of Spheres, *A. I. Ch. E. Journal*, **8**, 359-361 (1962).

21. Hong, T.T., Yamada, Y. and Tien, C.L., Effects of Non-Darcian and Non-Uniform Porosity on Vertical-Plate Natural Convection in Porous Media, *J. Heat Transfer*, **109**, 356-362 (1987).

22. Vafai, K. and Tien, C.L., Boundary and Inertia Effects on Flow and Heat Transfer in Porous Media, *Int. J. Heat Mass Transfer*, **24**, 195-203 (1981).

23. Tokunaga, Tetsu K., Laboratory Permeability Errors from Annular Wall Flow, *Soil Science Am. J.*, **52**, 24-27 (1988).

24. Hong, J.T. and Tien, C.L., Analysis of Thermal Dispersion Effect on Vertical-Plate Natural Convection in Porous Media, *Int. J. Heat Mass Transfer*, **30**, 143-150 (1987).

25. Fournier, R.O. and Potter, R.W., An Equation Correlating the Solubility of Quartz in Water from 25 °C to 900 °C at Pressures up to 10,000 Bars, *Geochimica et Cosmochimica Acta*, **46**, 1969-1973 (1982).

26. Verma, A. and Pruess, K., Thermohydrological Conditions and Silica Redistribution Near High-Level Nuclear Wastes Emplaced in Saturated Geological Formations, *J. of Geophys. Res.*, **93**, 1159-1173 (1988).

Table 1 - Parameters used in Reference Case

Temperature of wire, T:	377 °C
Temperature of outer wall, T_o:	375 °C
Average pressure, $\bar{P}$	225 bars (22.5 MPa)
Permeability, k	40 Darcies (40×10^{-12} m^2)
Porosity, ϕ	.25
Cylinder radius, R	0.0381 m
Cylinder height, H	0.2286 m
Aspect ratio (R:H)	1:6
Computational grid (see Figure 3)	21×15
Pressure and temperature spacings for thermophysical properties tabulation	.1 bar ×.1°C

Rock Properties

Rock heat capacity, C_{pR}	960 kJ/kg-°C
Rock density, ρ_R	2400 kg/m^3
Rock thermal conductivity, λ_R	3.35 W/m °C

Fluid Properties and Porous Medium Properties at 376 °C, 225 bars

Fluid heat capacity, C_{pf}	171.7 kJ/kg · °C
Fluid density, ρ_f	254.8 kg/m^3
Fluid thermal conductivity, λ_f	.426 W/m °C
Porous medium thermal conductivity λ_m	2.59 W/m°C
Fluid thermal diffusivity, κ_f	9.738×10^{-9}m^2/s
Porous medium diffusivity, κ_m	5.918×10^{-8}m^2/s
Dynamic viscosity	3.385×10^{-5} Pa·s

Table 2
Discretization and Boundary Effects

Case	Description	Permeability, darcies (1 darcy = 1×10^{-12} m^2)	Nusselt number, Nu
1	(Reference case - see Table 1) Average pressure = 225.5 bar Temperature interval = 375 to 377 °C Table interval (.1 °C × .1 bar) Mesh 21 × 15	20 40	1.831 2.227
2	Same as case 1, but table interval = (1 bar × .05 °C)	20 40	1.854 2.056
3	Same as case 2, but top and bottom boundaries are at constant T of 375 °C	20 40	1.738 2.077
4	Average pressure = 230 bar Temperature interval = 377 - 379 °C Table interval = (1 bar × .05 °C) Mesh = 20 × 15 (the 2 columns of grid blocks closest to heater wire were combined)	1 10 20 40	1.039 1.211 1.399 1.694
5	Same as case 4, but mesh = 21 × 15	40	1.493

Table 3
Aspect Ratio Effects

Case	Description	Permeability, darcies (1 darcy = $1 \times 10^{-12} m^2$)	Nusselt number, Nu
2	Same as case #2 (See Table 2) Aspect ratio (R:H) = 1:6	20 40	1.854 2.056
A1	Aspect ratio 1:3	10 20 40	1.795 2.182 2.742
A2	Aspect ratio 1:2	10 20 40	1.945 2.428 3.150
A3	Aspect ratio 1:1	10 20 40	2.198 2.895 3.956
A4	Aspect ratio 2:1	10 20 40	2.313 3.227 4.794

Table 4
Effect of Temperature Interval

Case	Description	Permeability Darcies (1 Darcy = $1 \times 10^{-12} m^2$)	Nusselt number, Nu
1	(Reference Case - see tables 1 & 2)	20 40	1.831 2.227
T10	Temperature interval 370° - 380°C	20 40	1.290 1.531
T1	Temperature interval 375.3° - 376.3°	20 40	1.732 2.153

Table 5
Effects of Average Temperature

Case	Temperature Interval, °C (Note: Description is the same as for case 1 in Tables 1 and 2)	Permeability Darcies	Nusselt Number Nu
T370	369-371	20 40	1.0021 1.0060
T372	371-373	20 40	1.0046 1.0137
T374	373-375	20 40	1.0203 1.0576
T375	374-376	20 40	1.1505 1.3348
T376 Reference Case 1	375-377	20 40	1.8307 2.2270
T377	376-378	20 40	1.2710 1.4340
T378	377-379	20 40	1.0312 1.0817
T380	379-381	20 40	1.0023 1.0066
TC377	376-378 P = 228.6 bar	40	1.8575
TC378	377-379 P = 231.25 bar	40	1.8197
TC380	379-381 P = 236.45 bar	40	1.6314

Table 6
Effects of Dispersion and Flow Channeling

Case	Description	Permeability	Nu
1	(Reference case - see Table 1)	40	2.227
D1	w/Dispersion	40	2.580
FC1	w/Flow channeling	40	2.609
DFC1	w/Dispersion and flow channeling	40	3.170

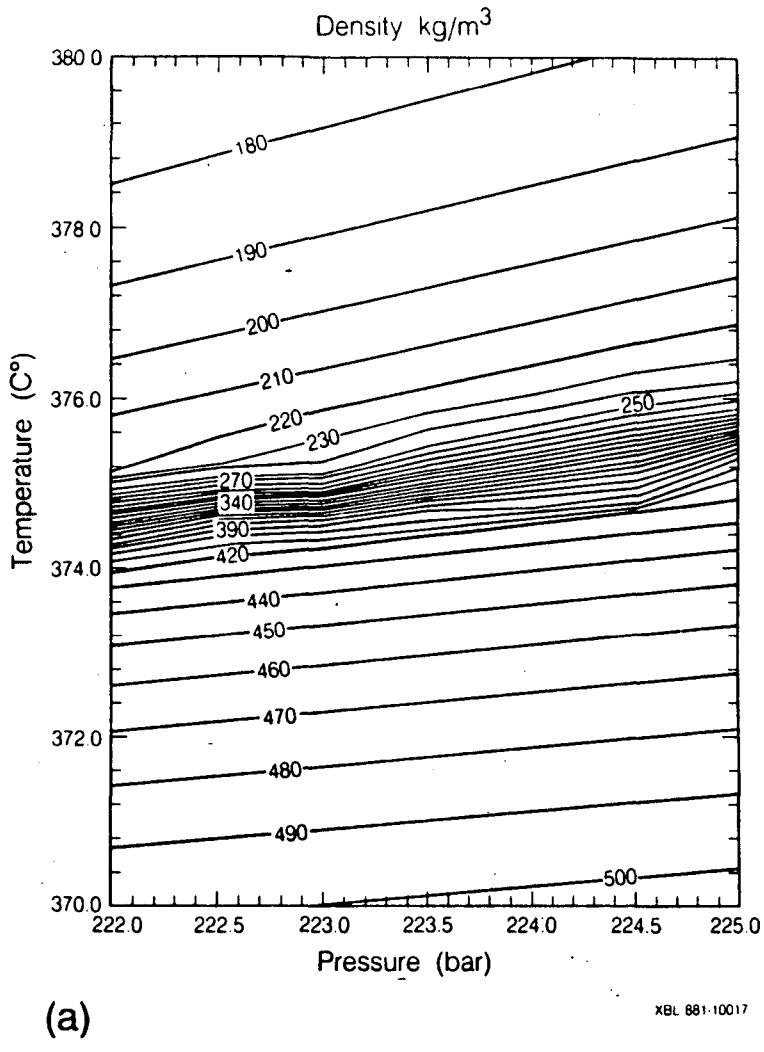

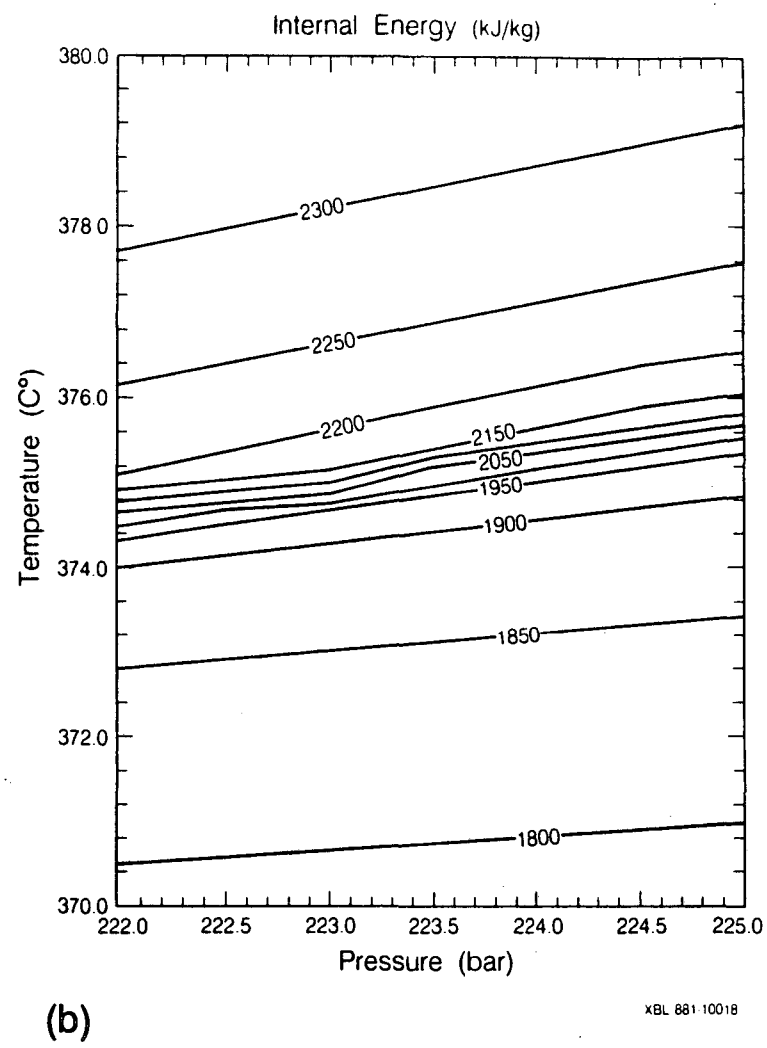

Figure 1. Contours of (a) density (kg/m^3) and (b) internal energy (kJ/kg) for pure water in the critical region.

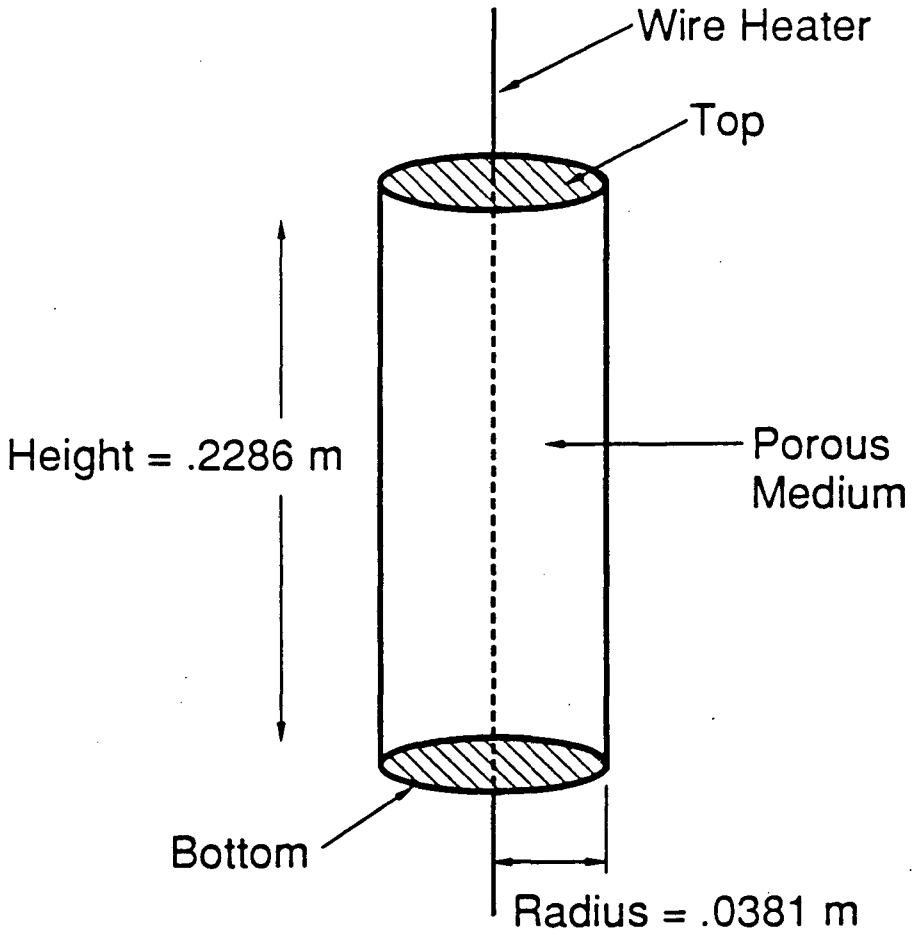

Figure 2. Cylindrical geometry for heat transfer study.

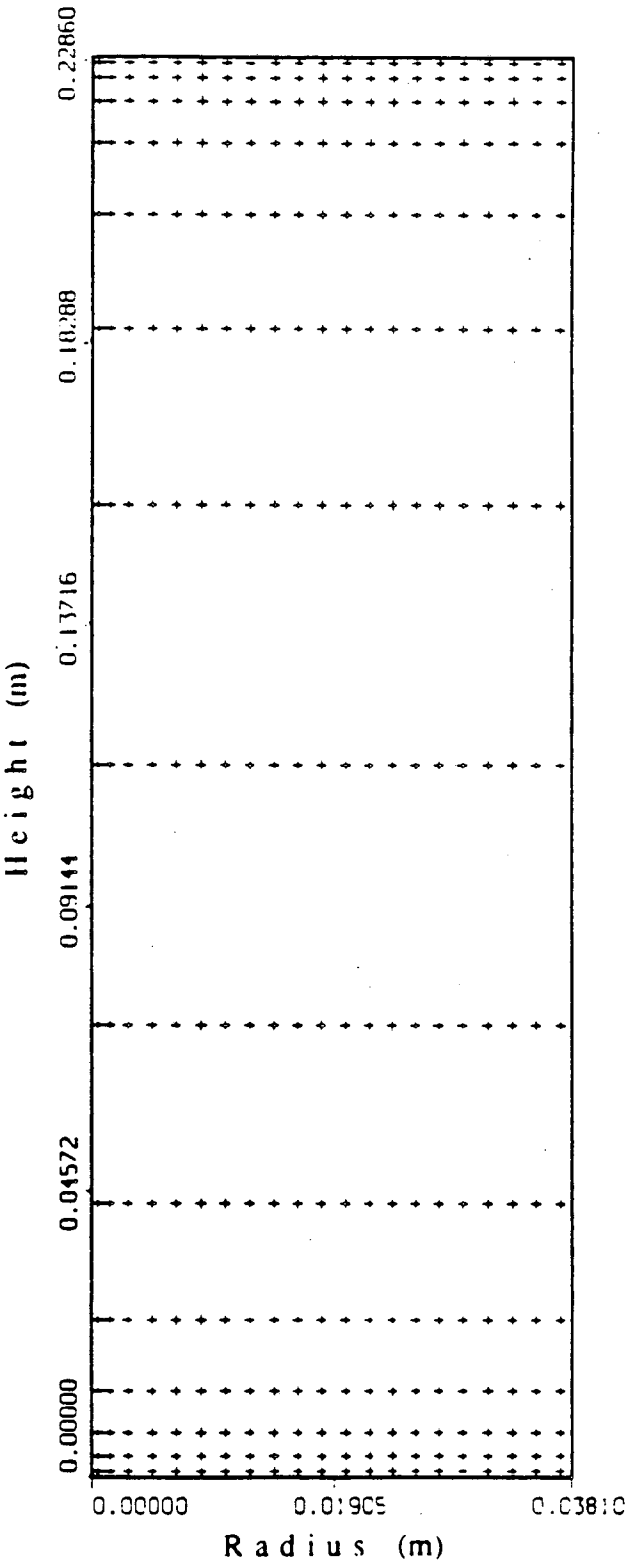

XBL 887-2660

Figure 3. Radial mesh geometry used in simulations. Left hand side of figure is axis of symmetry.

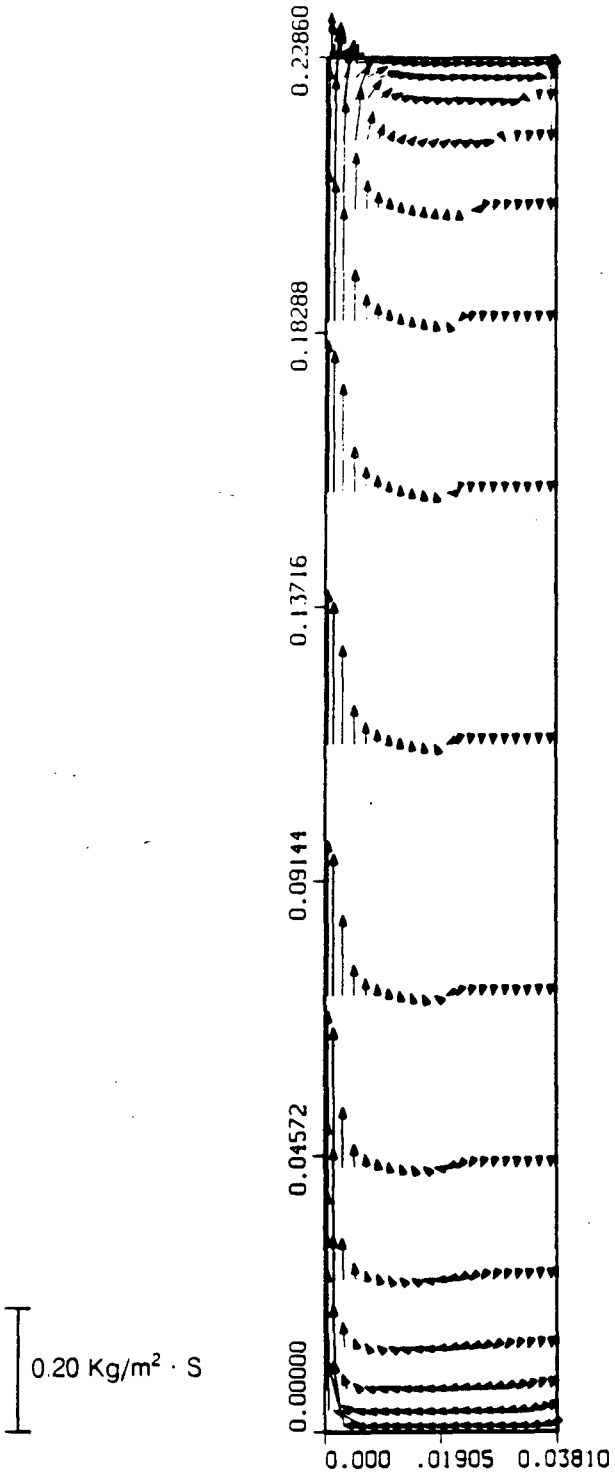

Figure 4. Typical fluid flux vectors (reference case) resulting from simulations of natural convection near the critical point.

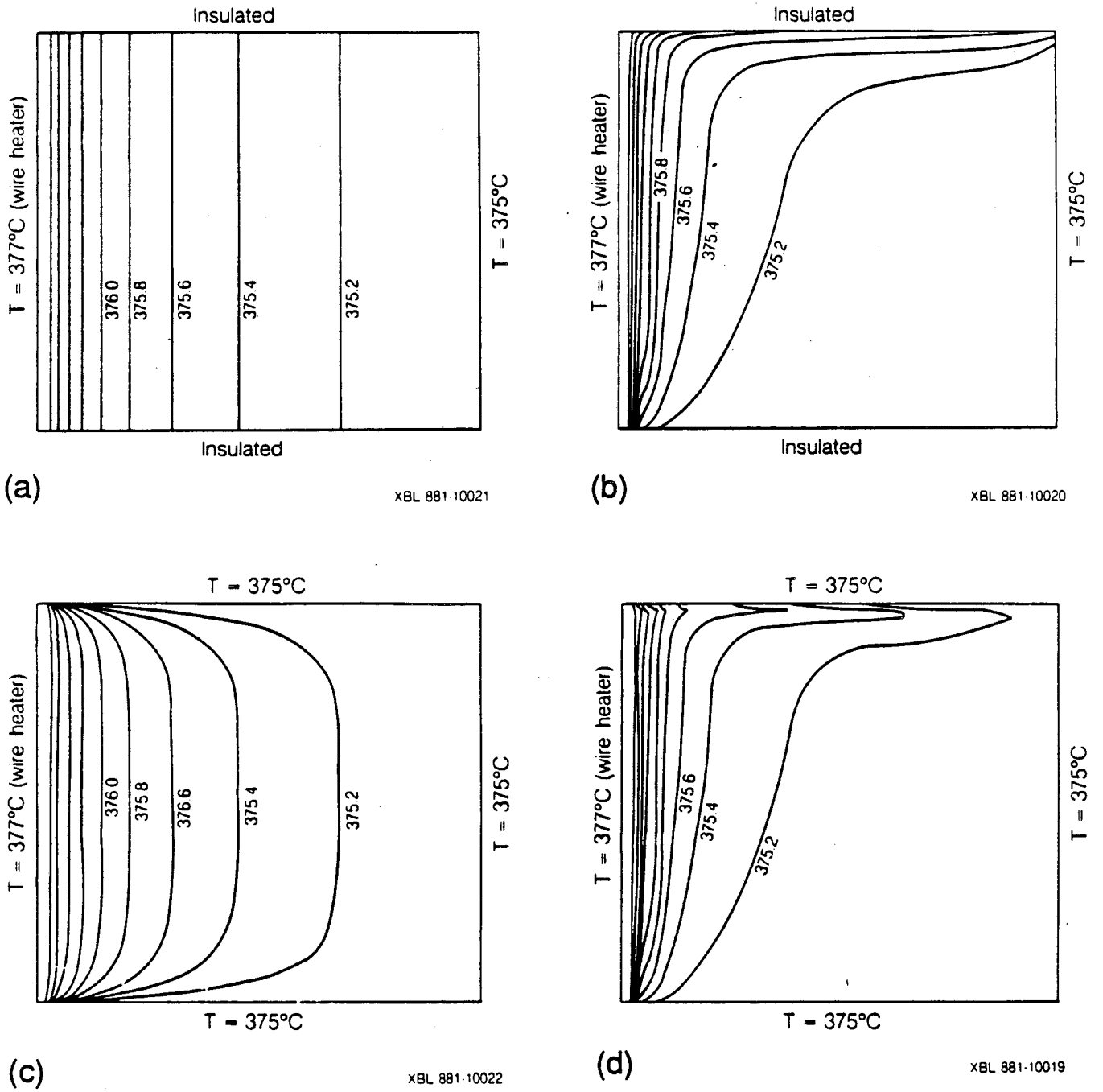

Figure 5. Isotherms for (a) case 2, conduction only, (b) case 2, with convection, (c) case 3, conduction only, and (d) case 3, with convection. The radial dimension is exaggerated 6 times.

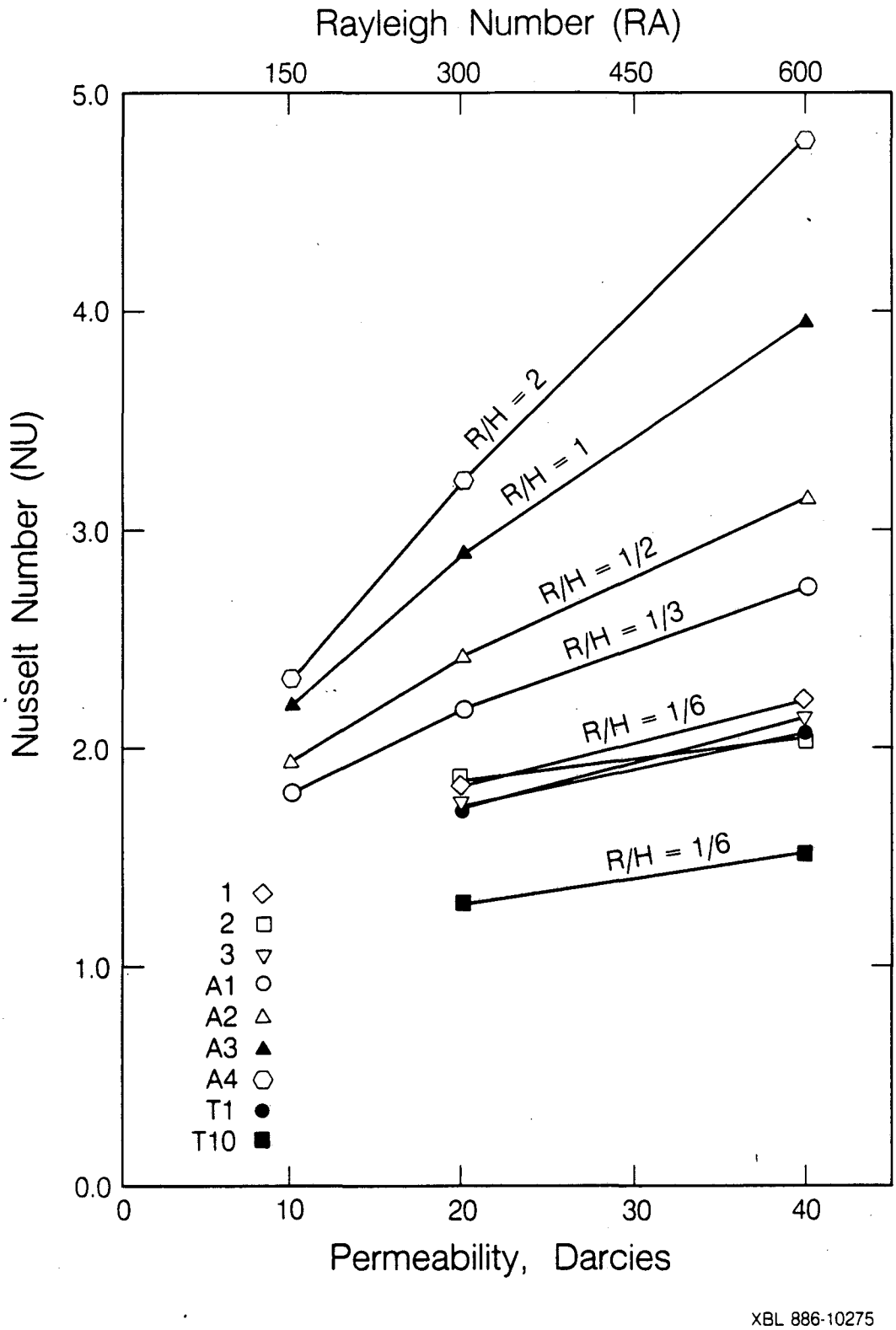

Figure 6. Results of near-critical convection simulations, plotted in terms of Nusselt number versus permeability (cases described in Table 3).

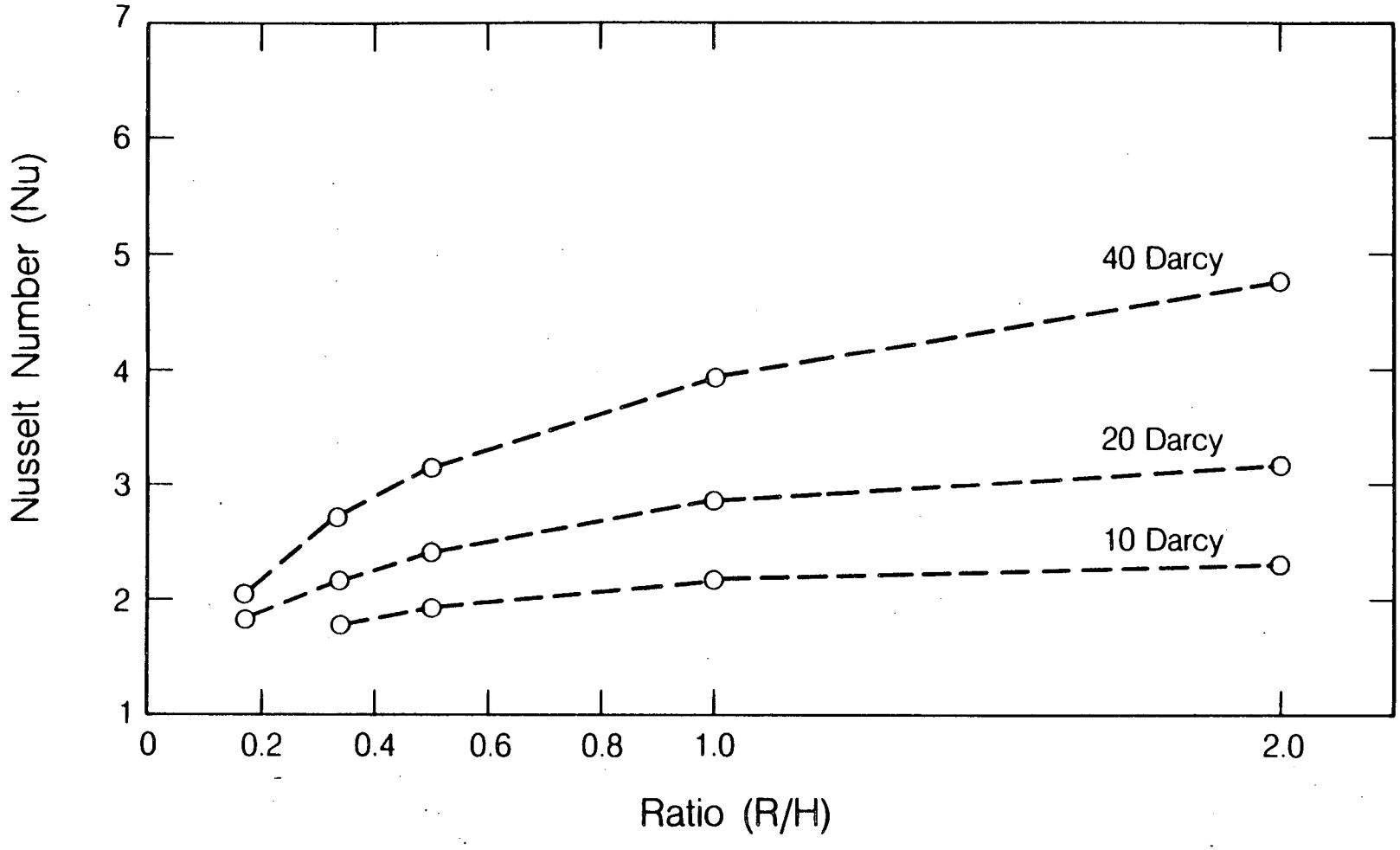

Figure 7. Results of near-critical convection simulations plotted in terms of Nusselt number versus aspect ratio (R/H).

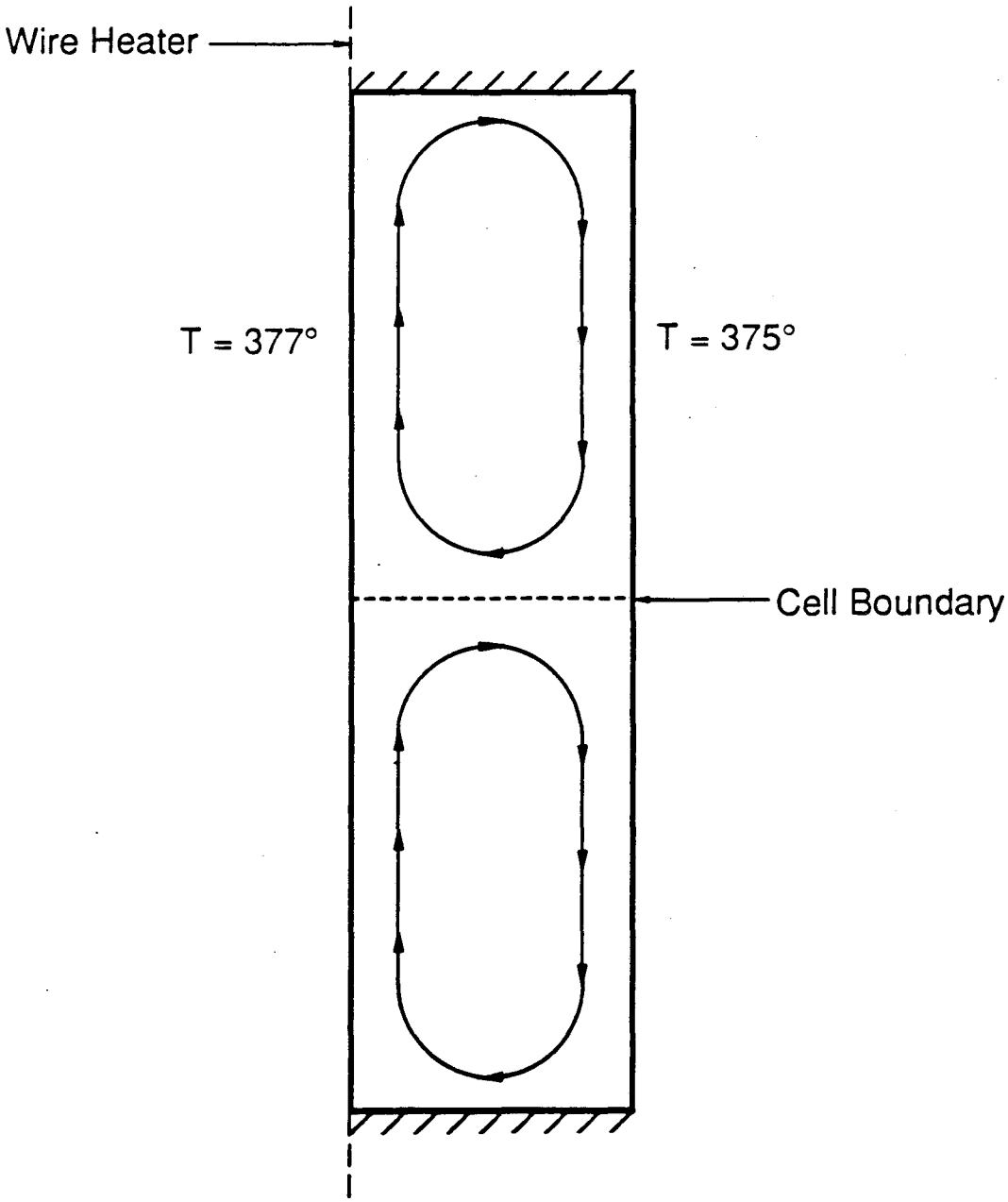

Figure 8. Conceptualization of two stacked convection cells.

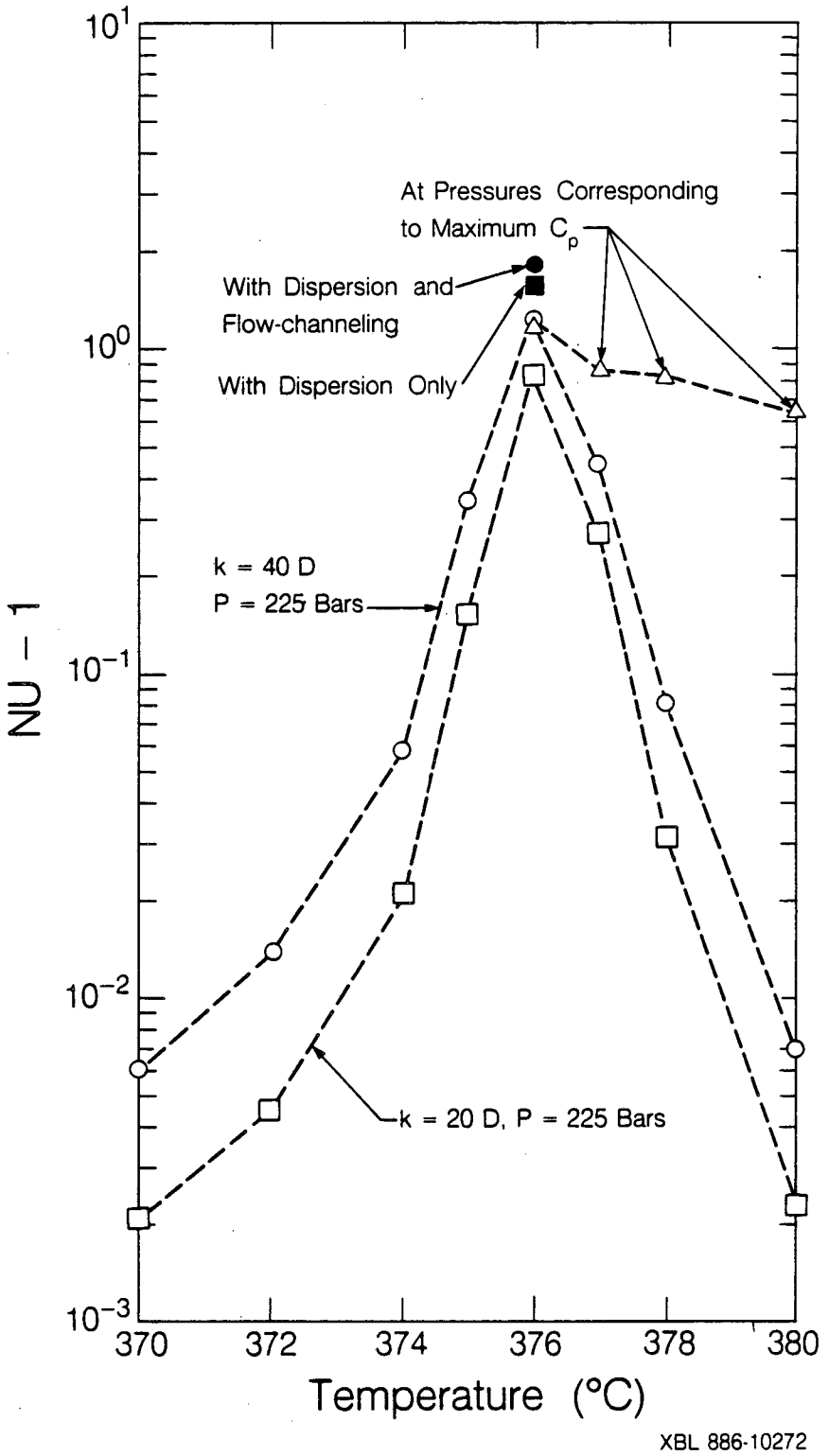

Figure 9. Results of near-critical convection simulations, plotted as (Nu-1) versus average temperature, for 20 and 40 darcy permeability. The temperature interval is 2 °C.

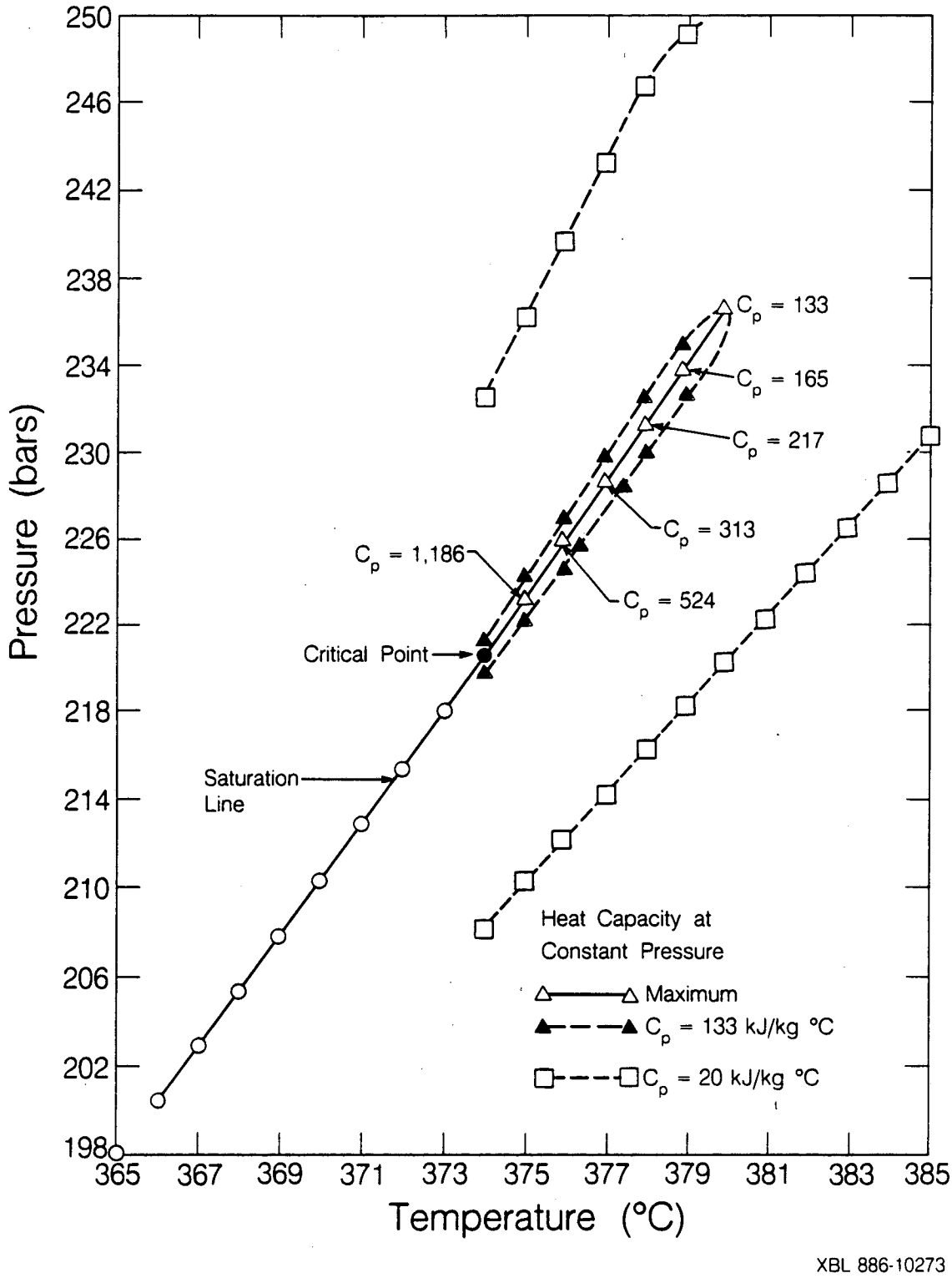

Figure 10. **Specific heat at constant pressure in the near-critical region.**

LAWRENCE BERKELEY LABORATORY
TECHNICAL INFORMATION DEPARTMENT
UNIVERSITY OF CALIFORNIA
BERKELEY, CALIFORNIA 94720